

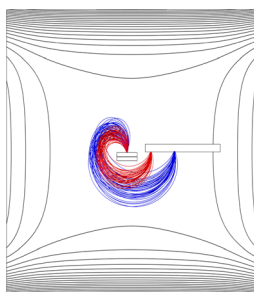
# Effects of Magnetic and Electric Field Uniformity on Coded Aperture Imaging Quality in a Cycloidal Mass Analyzer

David M. W. Landry,<sup>1</sup> William Kim,<sup>1</sup> Jason J. Amsden,<sup>1</sup> Shane T. Di Dona,<sup>1</sup> Heeju Choi,<sup>2</sup> Lori Haley,<sup>2</sup> Zachary E. Russell,<sup>1,3</sup> Charles B. Parker,<sup>1</sup> Jeffrey T. Glass,<sup>1</sup> Michael E. Gehm<sup>1</sup>

<sup>1</sup>Department of Electrical and Computer Engineering, Duke University, Durham, NC 27708, USA

<sup>2</sup>Electron Energy Corporation, Landisville, PA 17538, USA

<sup>3</sup>Present Address: Ion Innovations, Peachtree Corners, GA 30092, USA



**Abstract.** Cycloidal mass analyzers are unique sector mass analyzers as they exhibit perfect double focusing, making them ideal for incorporating spatial aperture coding, which can increase the throughput of a mass analyzer without affecting the resolving power. However, the focusing properties of the cycloidal mass analyzer depend on the uniformity of the electric and magnetic fields. In this paper, finite element simulation and charged particle tracing were used to investigate the effect of field uniformity on imaging performance of a cycloidal mass analyzer. For the magnetic field, we evaluate a new permanent magnet geometry by comparing it to a traditional geometry. Results indicate that creating an aperture image in a cycloidal mass spectrometer with the same FWHM as the slit requires less than 1% variation in magnetic field

strength along the ion trajectories. The new magnet design, called the opposed dipole magnet, has less than 1% field variation over an area approximately 62 × 65 mm; nearly twice the area available in a traditional design of similar size and weight. This allows ion imaging across larger detector arrays without loss of resolving power. In addition, we compare the aperture imaging quality of a traditionally used cycloidal mass spectrometer electric design with a new optimized design with improved field uniformity.

**Keywords:** Electric sector, Cycloidal mass analyzer, Aperture coding, Miniature mass spectrometer, Permanent magnet

Received: 28 April 2017/Revised: 21 September 2017/Accepted: 29 September 2017/Published Online: 23 October 2017

## Introduction

In miniaturization of a sector mass spectrometer, one traditionally encounters a tradeoff between throughput and resolution. One can either achieve high throughput (with low resolution), or high resolution (with low throughput), but not both. Building on research in X-ray imaging for space telescopes [1], optical spectroscopy, and conventional optical cameras [2, 3], a recent solution to this tradeoff has been demonstrated in sector mass spectrometry through the use of spatially coded apertures [4–6]. Spatial aperture coding replaces the single slit in a traditional sector spectrometer with an array of

slits. The size of the smallest slit in the array adjusts the resolving power whereas the total open area determines the throughput. Traditional spectra can then be computationally reconstructed, given knowledge of the aperture pattern and physics of the mass analyzer [7]. Chen et al. demonstrated an order of magnitude signal gain without loss in resolving power using a 90° magnetic sector [4, 5]. Furthermore, Russell et al. demonstrated the compatibility of aperture coding with the Mattauch-Herzog sector mass analyzer. However, the resulting image of the coded aperture was relatively poor due to fringing fields and the narrow width of the electric sector [6].

The cycloidal mass spectrometer is a sector instrument with orthogonal electric and magnetic fields first introduced in 1938 [8]. The electric field and ion travel paths are coplanar. As governed by the Lorentz force, the perpendicular magnetic field induces circular motion on the ions. The electric field affects the kinetic energy of the ions. Combined, the fields

David M. W. Landry and William Kim contributed equally to this work.

Correspondence to: Michael Gehm; e-mail: michael.gehm@duke.edu

induce cycloidal trajectories. Given uniform fields  $\vec{E} = \hat{y}E_0$  and  $\vec{B} = -\hat{z}B_0$ , the following can be derived from the equations of motion:

$$x = 2\pi \frac{m E_0}{z B_0^2} + x_0$$

where  $m/z$  is the mass to charge ratio of the ion,  $x$  is displacement between the ion source and detector along the x-axis, and  $x_0$  is the location of the ion source on the x-axis. For a given set of fields, ions are separated linearly on the detector, independent of their initial energy or launch angle. In other words, the sector is double focusing to all orders. This is ideal for imaging a spatially coded aperture onto a detector [7].

The unique focusing properties of the cycloidal mass analyzer depend on having highly uniform fields. In 1956, Robinson published a theoretical study showing the effects of field gradients on the cycloidal mass spectrometer [9]. For a completely uniform electric field, the focal plane is aligned with the plane of the ion source exit slit. A uniform gradient in the electric field shifts the focal plane above or below the plane of the ion source exit slit, while a uniform gradient in the magnetic field rotates the focal plane. For an ion imaging system, these field perturbations blur the image captured by the detector. With aperture coding, a blurred image can make reconstruction more difficult and lower the resolving power.

This paper investigates via finite element analysis and charged particle tracing the effects of electric and magnetic field uniformity on cycloidal mass analyzer coded aperture imaging quality. First, a magnet geometry similar to those used in previously reported cycloidal mass analyzers is compared with a new magnet geometry with similar size and weight but exhibiting improved field uniformity. The new magnet assembly was also fabricated and used to experimentally verify the simulated field profile. Second, two different electric sector configurations were investigated by adjusting the size, shape, and location of the electrodes using the magnetic field from the new magnet geometry. These simulations use the same magnet and electric sector configurations as reported in an experimental proof of concept system reported by Amsden et al. [10].

## Simulation Details

We performed simulations in COMSOL ver. 5.2a using the AC/DC and Charged Particle Tracing modules. The AC/DC module calculates the magnetostatic and electrostatic fields, while the Charged Particle Tracing module simulates ions traveling through the mass analyzer. We first simulated and compared the magnet assembly changes. Then we used simulations to optimize the electric sector design using the new magnet assembly field.

To reduce computation time while maintaining high fidelity in the regions of interest, the ion travel plane is meshed more finely than the remainder of the geometric model. The ion

travel plane is meshed with a minimum element size of 5  $\mu\text{m}$  and a maximum element size of 0.5 mm. The volume around this plane contains mesh elements between 1 and 80 mm in size. The magnet assemblies are meshed with elements between 14.4 and 80 mm in size. A box extends more than 300 mm beyond the magnet assembly in every direction with mesh elements ranging in size from 56 to 400 mm. It is important to note that this bounding box must be sufficiently large to prevent the edges of the simulation from affecting the field simulation. We determined the size of the bounding box by increasing its size until further increases no longer affected the simulated field.

## Magnetic Field Simulations

Two types of materials comprise the magnet geometric models: annealed grade 416 stainless steel (SS) and the rare earth permanent magnet Nd-Fe-B. Material properties for the 416 SS were obtained from the nonlinear magnetic materials library in COMSOL. The library defines a B-H curve for the material, which allows for more accurate calculations than using a single permeability value. This also allows COMSOL to simulate magnetic saturation of the material. The Nd-Fe-B magnet, grade N50, is defined with a remnant flux density  $B_r$  of 1.4 T and minimum coercivity of 923 kA/m.

## Electric Field Simulations

The electric model assumes copper electrodes, with material properties obtained from the COMSOL materials library. Using the electrostatic physics interface in COMSOL, electrode voltages were assigned to the model to generate a constant value electric field along the region of interest.

## Charged Particle Tracing Simulations

Simulated ion trajectories were used to evaluate the quality of the new magnetic and electric sectors. To isolate the effect of the magnetic field, the magnet array results assume a completely uniform electric field of 706 V/m. This field strength was selected in accordance with the cycloidal mass analyzer prototype, described in a separate paper [10]. Electric sector results use simulated magnetic *and* electric fields.

To simulate ion trajectories, singly and doubly charged argon with mass to charge ratios of  $m/z = 40$  and 20, respectively, were emitted from an ion source with an aperture at the geometric center of the magnet. The aperture is spatially coded with a modified S11 pattern, a binary Hadamard code [11]. The pattern consists of three slits. It has overall dimensions of  $550 \times 350 \mu\text{m}$ , with a total open area of  $300 \times 350 \mu\text{m}$ . Its smallest feature is  $50 \times 350 \mu\text{m}$ . The ions had energies of  $14 \pm 2 \text{ eV}$  in and an angular distribution of  $0.0 \pm 9.5^\circ$  in the x-y plane measured from the y-axis. The angular distribution in the y-z plane is  $0^\circ$ . Ions with mass to charge ratio of 20 and 40 were chosen as they reach opposite ends of the detector array used in the cycloidal mass analyzer proof of concept reported by Amsden et al in a separate paper [10]. The initial energy and

angular dispersion values correspond to those measured in an ion source described by Amsden et al. [10].

## Results

Results for the magnet assemblies and electric sector configurations are split into two sections. Each section compares a more uniform design with a similar, commonly used design. To evaluate the effect of the fields on imaging performance, ion trajectories were simulated. To separate the effects of magnetic field uniformity and electric field uniformity on aperture imaging, simulations of the two magnet geometries assume a uniform electric field. Simulations of the two electric sector configurations use the magnetic field from the new magnet geometry with improved field uniformity.

### Magnet Assembly Results

This section discusses the differences in aperture image quality and magnetic field uniformity of two different permanent magnet geometries. The first is a magnet geometry similar to those in previous reports of cycloidal mass analyzers [12–15] as well as permanent magnet desktop magnetic resonance imagers [16]. This assembly is often called an H-shaped magnet because the magnetic flux lines through a cross-section resemble the letter H. The second is a new geometry that shows improved imaging quality with a similar size and weight as the H-magnet. We call this an “opposed dipole magnet” because the magnetic field in the gap is opposite in direction to the magnetization of the bar magnets. Details of these geometries and their effect on field uniformity and aperture imaging are described in the following section.

*H-Shaped Magnet* This section presents the H-shaped magnet design, field profile simulation, and ion trajectory simulation results.

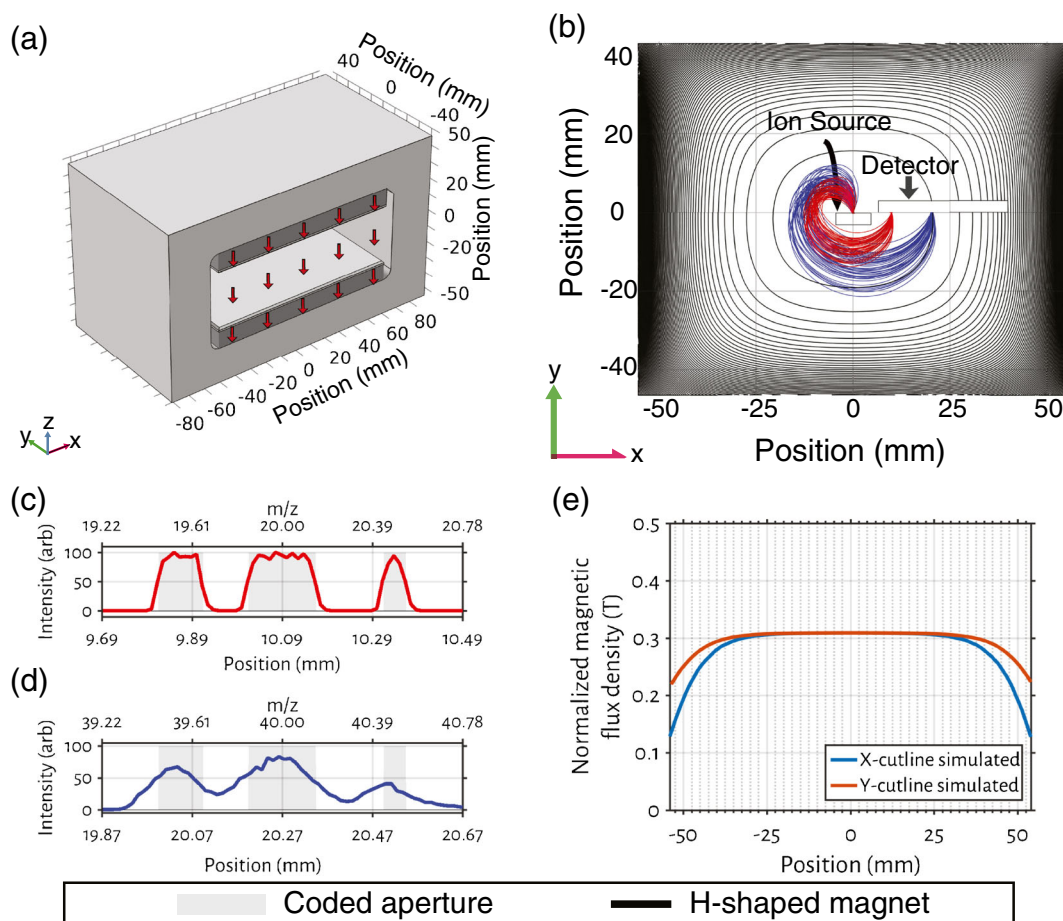
### H-Shaped Magnet Design

Figure 1a shows the geometric model of the H-shaped magnet. The model is comprised of two Nd-Fe-B permanent magnets, two inner-facing pole pieces of 416 SS, and a 416 SS yoke that wraps around the structure, connecting the two magnets. The Nd-Fe-B magnet is magnetized in the -z-direction, producing a -z-direction field in the gap between them. The 416 SS is shown as light grey, and Nd-Fe-B magnets are shown as dark grey. Red arrows denote the direction of the magnetic flux lines. The outer dimensions of the yoke and assembly are 170 × 90 × 100 mm. The enclosed field region is 110 × 90 mm in the x-y plane. The magnets are 10 mm thick. The pole pieces are 2 mm thick with chamfered edges. The gap between pole pieces is 35 mm. Based on the volume and density of materials, the assembly weighs approximately 9 kg.

### H-Shaped Magnet Results

Figure 1b through e shows the COMSOL simulation results. The figure presents (b) ion trajectories and contour plot of field strength in the x-y plane, (c) simulated detector readings zoomed and centered on  $m/z$  of 20, and (d)  $m/z$  of 40, and (e) field profiles along the x- and y-axes. Figure 1e shows the field strengths along the x- and y-axes, centered in the middle of the ion travel region (i.e.,  $z = 0$  plane). The assembly has a peak field of 0.3 T. The field strength varies less than 1% across a region of 43 × 46 mm and drops rapidly outside this region. Across the entire extent, field strength varies by 29% and 52% for x- and y-axes, respectively. Figure 1b plots a plane cut through the center of the ion travel region ( $z = 0$ ). Contour lines show field strength in increments 1% of peak strength. The strongest part of the field is in the center. Figure 1b also shows ion trajectories as black lines starting at the aperture at the top of the ion source to the detector. Differing initial energies and angles cause each ion to follow a different path through the field (distributions given above). Figure 1b illustrates the degree of field non-uniformity and the resulting ion trajectories for both  $m/z$ . All 20  $m/z$  ions remained inside the 1% contour line. However, several 40  $m/z$  ion trajectories extend beyond the 1% contour line. To investigate the aperture imaging quality, we examined where each ion crossed the detector plane and simulated a detector reading by plotting a histogram, binning ion locations to match the detector in the experimental apparatus. The detector has 1704 detection elements along the length of the x-axis. Each element is 12 μm × 3 mm. The histogram was normalized to a peak value of 100. Figure 1c plots the simulated detector reading centered on where the ions with  $m/z$  of 20 strike the detector. The signal returns to baseline following the aperture pattern. A simulation with a 50 μm slit produced an image with a FWHM of approximately 50 μm (data not shown), indicating good imaging quality. Figure 1d presents the same simulated detector reading centered where ions with  $m/z$  of 40 strike the detector. Although the signal follows the general aperture pattern, the signal is blurred to the point that it does not return to baseline between the slits in the aperture pattern. A simulation with just a single 50 μm slit produced an image with a FWHM of 113 μm (data not shown). In summary, aperture imaging quality was good for  $m/z$  of 20. However, aperture imaging quality for  $m/z$  of 40 was relatively poor. The main difference between the 20 and 40  $m/z$  ion trajectories is that the 40  $m/z$  trajectories cover a larger area, where the magnetic field varies by >1%. Therefore, we conclude that, assuming a uniform electric field, a magnetic field variation of <1% is required for good aperture imaging.

*Opposed Dipole Magnet* We investigated several approaches to keep field variation under 1%. The most straightforward is to increase the size of the H-shaped magnet. Its uniform region is proportional to its overall size. However, this would produce a magnet that is significantly heavier. Another method is to



**Figure 1.** (a) CAD model of the H-shaped magnetic array. Light grey indicates magnetic stainless steel, dark grey items are Nd-Fe-B magnets, and red arrows indicate the direction of the magnetic field. (b) A plane through the ion travel region simulated ion trajectories overlay a contour plot of the magnetic field strength in 1% steps of peak field. The ion trajectories have  $m/z$  of 20 (red) and 40 (blue). (c) A histogram simulating a detector reading centered at  $m/z$  of 20. Gray boxes indicate the aperture pattern. For reference, an  $m/z$  axis is included. (d) Same as (c), but centered at  $m/z$  of 40. (e) Magnetic field profiles along the x- and y-axes

leverage Halbach or Stelter arrays [17–19]. These designs create uniform fields, but are heavy and complicated to fabricate. A third method is a cylindrical assembly claiming better field uniformity without the added weight of a larger H-shaped magnet or fabrication complexity of Halbach and Stelter arrays [20]. Unfortunately, this cylindrical assembly is difficult to incorporate into a cycloidal mass analyzer as there is no opening for inserting and removing the electric sector, ion source, and detector.

The cylindrical design approach was modified to accommodate the requirements of the cycloidal analyzer, resulting in the opposed dipole assembly presented below. The cylindrical assembly induces a uniform field because of the interaction between a ring magnet and its upper and lower face plates. In place of ring magnets, our design uses parallel bar magnets. This creates an accessible gap at the expense of some uniformity. The new assembly provides a field significantly more uniform than a similar-sized H-shaped magnet, but maintains the interior space accessibility of an H-shaped magnet design.

### Opposed Dipole Magnet Design

Figure 2a shows the geometric model of the new assembly. The model is composed of two Nd-Fe-B permanent magnets and two 416 SS plates to conduct the magnetic flux. Stainless steel materials are shown as light grey. Nd-Fe-B magnets are shown as dark grey. Red arrows denote the direction of the magnetic flux lines. The Nd-Fe-B magnets are magnetized in the  $+z$ -direction, and with the SS plates, produce a  $-z$ -direction field in the ion travel region. In contrast to the H-shaped magnet, here the Nd-Fe-B is magnetized antiparallel to the direction of the field in the gap. Thus we name this geometry an opposed dipole. The outer dimensions of the assembly are  $194 \times 110 \times 69$  mm. The enclosed field region is  $110 \times 110 \times 35$  mm. The magnets are each  $42 \times 110 \times 35$  mm. Based on the volume and density of the materials, the entire assembly weighs approximately 8 kg. These dimensions were chosen to match the magnet constructed for the experimental proof of concept reported in Amsden et. al. [10].

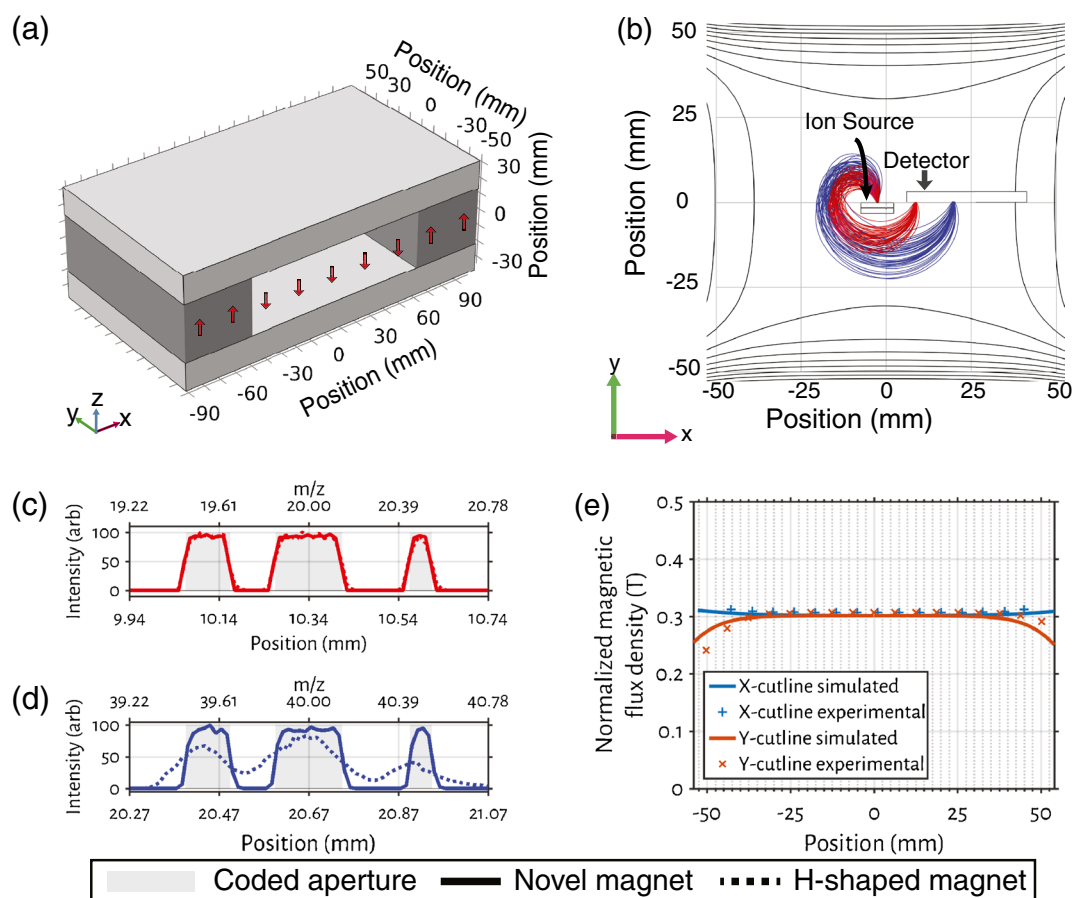


**Figure 2.** (a) Opposed dipole magnetic array CAD model – light grey indicates magnetic stainless steel, dark grey items are Nd-Fe-B magnets, and red arrows indicate the direction of the magnetic field. (b) A plane through the ion travel region simulated ion trajectories overlay a contour plot of the magnetic field strength in 1% steps of peak field. The ion trajectories have an  $m/z$  of 20 (red) and 40 (blue). (c) A histogram simulating a detector reading centered at  $m/z$  of 20. Gray boxes indicate the aperture pattern. For reference, included are an  $m/z$  axis and the corresponding H-shaped magnet histogram (dotted line). (d) Same as (c), but centered at  $m/z$  of 40. (e) Magnetic field profiles along the x- and y-axes. Simulated profiles are solid lines. Experimental results are plotted as 'x's. For legibility, the experimental profiles only show a fifth of the points acquired

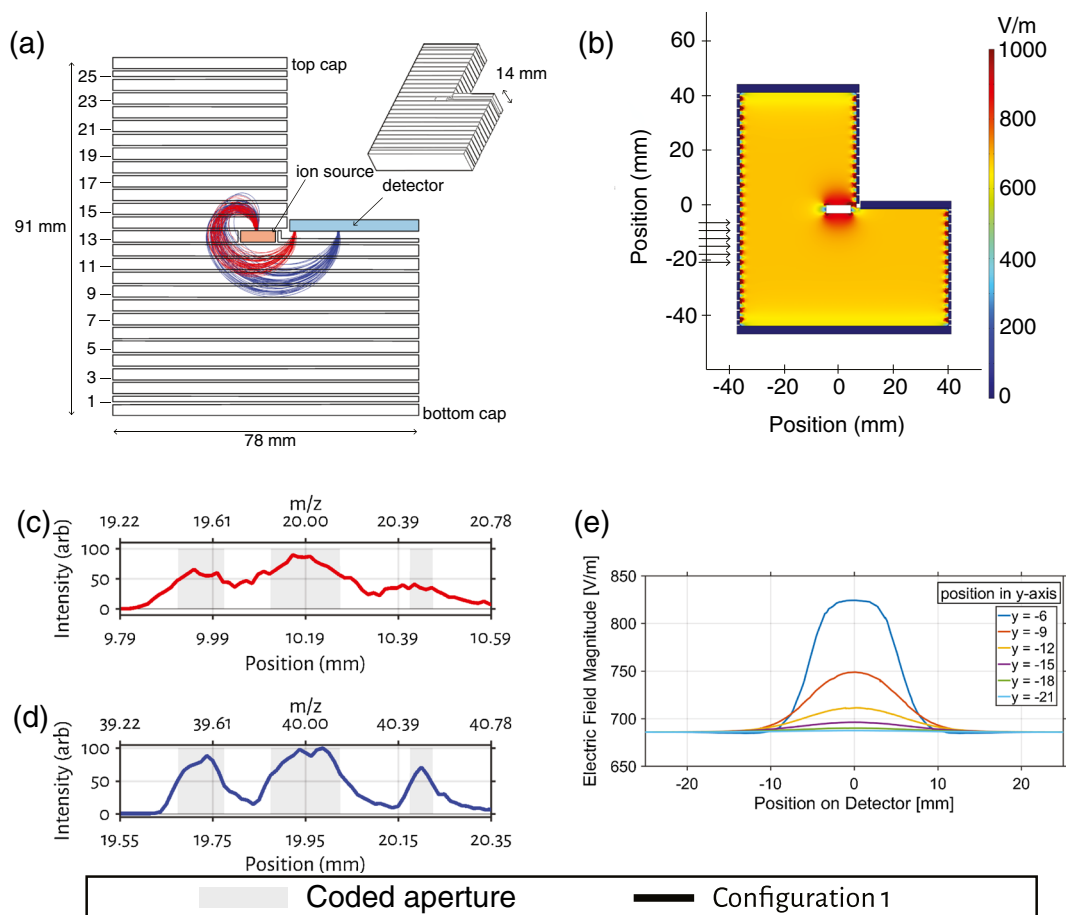
### Opposed Dipole Magnet Results

Figure 2e shows the field strengths along the x- and y-axes, centered in the middle of the ion travel region (i.e.,  $z = 0$  plane). Peak field is slightly larger than 0.3 T, located at the left and right extremes of the x-axis. The field strength varies less than 1% across a region  $62 \text{ mm} \times 65 \text{ mm}$ . Across the entire extent, field strength varies by 3% and 18% for x- and y-axes, respectively. Also shown are measurements from the fabricated design. To verify the simulations, we fabricated the opposed dipole magnet assembly and mapped the magnetic field (see Figure 2e) in the gap using a Lakeshore 460 Gaussmeter with 3-axis Hall probe mounted on the precision XYZ station, which is incorporated into a Labview real time data acquisition system. Experimental and simulated fields match closely along the x-axis. Along the y-axis, there is a slight asymmetry in the fabricated magnet due to slightly different properties in each of the bar magnets compared with the symmetrical simulated version. Figure 2b shows ion trajectories overlaid on simulated field contour lines. The contours indicate 1% steps in field strength. Like the H-shaped

magnet design, ions are modeled with initial angle and energy as described above. From this figure, we see that the ion trajectories for both the 20 and 40  $m/z$  ions are in a region in which the field varies by <1%. A detector reading was simulated with the same method as the H-shaped magnet. Figure 2c and d plot the detector signal centered at  $m/z$  of 20 and 40, respectively. With both, the signal returns to baseline between each slit following the aperture pattern. A simulation with a  $50 \text{ }\mu\text{m}$  slit produced  $50 \text{ }\mu\text{m}$  images at both  $m/z$  locations, indicating good imaging for both 20 and 40  $m/z$  ions and confirming that aperture imaging requires a magnetic field variation of <1%.

### Electric Sector Results

**Electric Sector Configuration 1** The first electric sector configuration investigated here has been utilized experimentally in a coded aperture miniature mass spectrometer described in a separate paper [10] and also similar to those previously reported in the literature [21]. The electric sector is an L-shaped box of dimensions  $91 \times 78 \times 14 \text{ mm}$ . Figure 3a shows a CAD model of



**Figure 3.** (a) Configuration 1 electric sector. Red lines represent  $m/z = 20$  ion trajectory whereas blue lines represent  $m/z = 40$  ion trajectory. (b) Electric field magnitude profile. (c) Configuration 1 imaging quality at detector for  $m/z = 20$ . (d) Configuration 1 imaging quality at detector for  $m/z = 40$ . (e) Configuration 1 electric field magnitude near ion source region

the first electric sector configuration. It is comprised of 25 parallel electrodes, spaced 0.5 mm apart. Each electrode encircles the ion travel region. Caps on the bottom and top are electrically connected to the first and last electrodes respectively. All but two electrodes are 3 mm wide. Next to the top and bottom caps, electrodes #1 and #25 are 1.5 mm wide. Around the ion source, electrode #13 is 3 mm wide to the left of the ion source, but reduces to 1 mm near the detector to allow positioning of the detector plane at the midpoint of the center electrode. The ion source is level with the neighboring electrodes, similar to the configuration discussed by Blasé et al. [21].

The electrodes are biased according to the following equation:

$$V_i = \left( \frac{i-13}{13} \right) Ed$$

where  $i$  represents the  $i^{\text{th}}$  electrode from the bottom (#0 to #25),  $d$  is the distance between the top and bottom cap, and  $E$  is the desired electric field. With this arrangement, the center electrode, #13, is at ground. The ion source and detector are aligned with the center electrode and are also held at ground.

Figure 3b shows a color map of the electric field magnitude in a slice through the center of the electric sector. The electric field is generally uniform, except near the top and bottom caps and near the ion source. Since ions do not pass through the non-uniformities near the top and bottom caps, it is unlikely that these regions affect aperture imaging. However, lower  $m/z$  ions pass through the non-uniform region surrounding the ion source, and every ion passes through the non-uniform field directly above the source.

Figure 3e shows a plot of the electric field magnitude along lines indicated by arrows in Figure 3b, in proximity to the ion source region. Ions with lower  $m/z$  trace a shorter path through the electric field. Since the ion trajectories with  $m/z$  of 20 are closer to the ion source, the particles are subject to more electric field non-uniformity. Thus, imaging for lower  $m/z$  ions is worse than that of higher  $m/z$  ions, as seen in Figure 3c and d.

Simulating ions with  $m/z$  of 20 and 40, this configuration yields aperture images at the detector as seen in Figure 3c and d, respectively. Figure 3c is the detector image for ions of  $m/z$  of 20. Figure 3d shows the detector image for ions of  $m/z$  of 40. Under ideal conditions, the detector image would perfectly match the aperture pattern, indicated by the grey boxes. With

this configuration, the aperture image is blurred slightly with the image centered at  $m/z$  of 20 more blurred than that at  $m/z$  of 40. The blurring in the coded aperture images is consistent with a simulation using a single  $50\ \mu\text{m}$  slit simulation. The single slit simulation produced an image with a FWHM of  $130\ \mu\text{m}$  at  $m/z$  of 20, and  $90\ \mu\text{m}$  for ions at  $m/z$  of 40 (data not shown). Given perfectly uniform fields, the image of the single slit would be  $50\ \mu\text{m}$  wide.

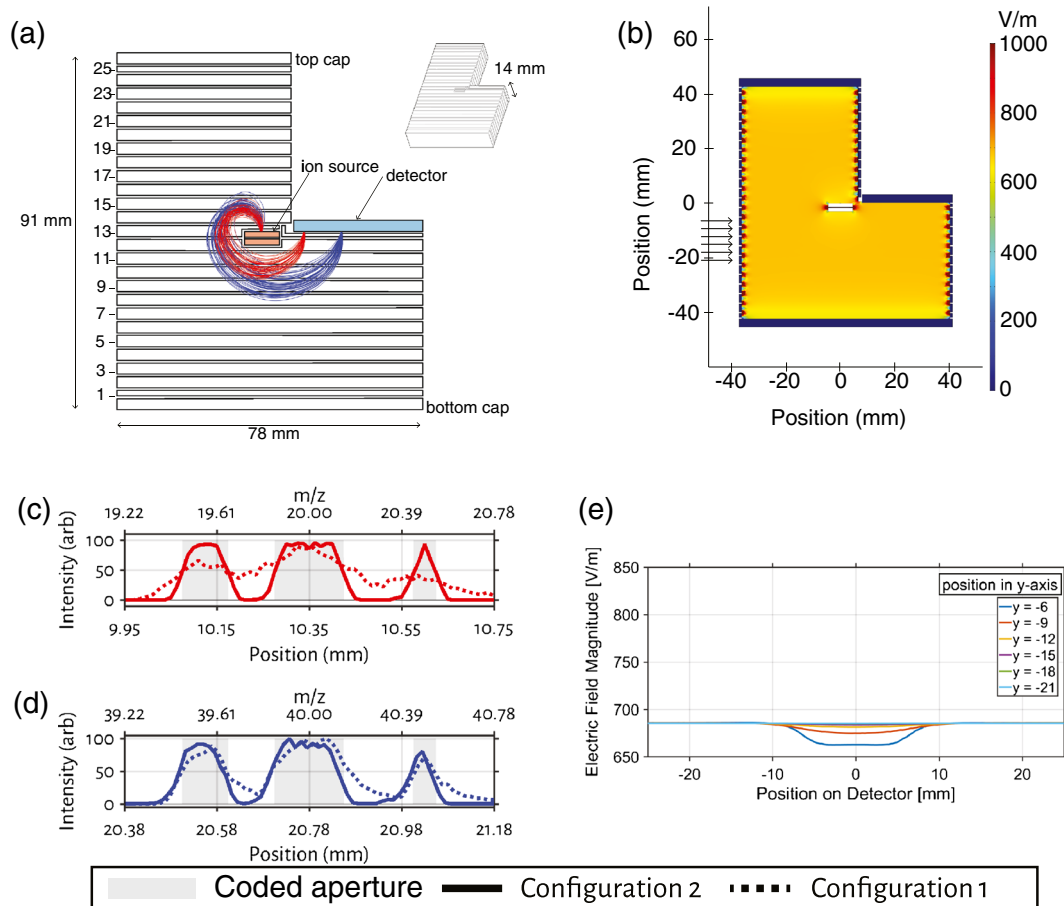
**Electric Sector Configuration 2** Although configuration 1 enabled imaging of a coded aperture, it was still limiting the instrument performance, including resolution, as seen in Figure 3a. After examining the electric field profile of configuration 1, we determined that the non-uniform electric field near the ion source likely blurred aperture imaging of ions at the lower end of the instrument  $m/z$  range. An improved configuration, configuration 2, was simulated to test this hypothesis by obtaining a quantitative assessment of imaging performance.

Figure 4a shows the optimized electric sector configuration. The overall design is similar to configuration 1. The sector is an L-shaped box of dimensions  $91 \times 78 \times 14\ \text{mm}$ . There are 25

electrodes, spaced  $0.5\ \text{mm}$  apart. Three of the electrodes are  $1.5\ \text{mm}$  wide, whereas the rest are  $3\ \text{mm}$  wide. The primary difference is that the ion source is now placed midway between neighboring electrodes. Additionally, the top and bottom of the ion source are biased at different voltages to match nearby electrodes. Applying different potentials to the top and bottom of the ion source could easily be accomplished using a multi-layer scaffold for the ion source such as low-temperature co-fired ceramics, as has been demonstrated previously [22]. The rest of the electrodes were biased in the same manner discussed in configuration 1.

This configuration yields the aperture pattern images seen in Figure 4b and c. This new configuration creates more focused aperture images. In particular, the ions with  $m/z$  20 (Figure 4b) are noticeably improved.

Figure 4a shows the electric field magnitude of the configuration 2 electric sector. Biasing the top and bottom of the ion source separately noticeably improves field uniformity. Figure 4b shows the electric field magnitude around the ion source. Each line is a cutline across the sector, Figure 4a. Note that although the field profile is not completely uniform, the variation is less than 5%. From the simulated detector readings,



**Figure 4.** (a) Configuration 2 electric sector. Red lines represent  $m/z = 20$  ion trajectory whereas blue lines represent  $m/z = 40$  ion trajectory. (b) Electric field magnitude profile. (c) Configurations 1 and 2 imaging quality at detector for  $m/z = 20$ . (d) Configurations 1 and 2 imaging quality at detector for  $m/z = 40$ . (e) Configuration 2 electric field magnitude near ion source region

configuration 2 creates consistently focused images across its entire mass range.

Although the image is noticeably improved, the lower end of the mass range still blurs more than the upper end. Repeating the single, 50  $\mu\text{m}$  slit simulation, the FWHM was 80  $\mu\text{m}$  and 60  $\mu\text{m}$ , for  $m/z$  of 20 and 40, respectively (data not shown), corresponding to an approximate 30% to 40% reduction in the FWHM compared with configuration 1.

## Discussion and Conclusion

This paper compares via simulation the coded aperture imaging quality using a magnet geometry and electric sector geometry traditionally used in cycloidal mass analyzers with a new magnet geometry and optimized electric sector with improved field uniformity.

Magnet assembly results indicate that achieving an aperture image FWHM similar to that of the slit requires magnetic field variation  $<1\%$  over the entire path of the ion. The traditional H-shaped magnet provided accurate imaging but only for a small range of mass to charge ratios due to the  $>1\%$  field variation over the ion trajectories. The opposed dipole magnet geometry was presented, a novel magnet geometry with improved uniformity and similar size and weight as traditional geometries. The opposed dipole magnet assembly allows for accurate aperture imaging for a significantly larger range of mass to charge ratios. In addition, to use with cycloidal mass analyzers with aperture coding, the new magnet design could also be integrated into cycloidal instruments where the electric field is scanned to acquire a spectrum. Furthermore, this geometry could be useful in other applications where a highly uniform field is desired, such as desktop magnetic resonance imaging.

The electric sector results indicate that placing the ion source midway between neighboring electrodes improves electric field uniformity near the ion source. This improves imaging performance in a cycloidal mass analyzer, particularly for lower  $m/z$  ions. This new configuration should improve the performance of any mass analyzer that relies on a uniform electric field profile.

## Acknowledgements

The information, data, or work presented herein was funded in part by the Advanced Research Projects Agency-Energy (ARPA-E), US Department of Energy, under Award Number DE-AR0000546. The views and opinions of authors expressed herein do not necessarily state or reflect those of the United States Government or any agency thereof.

## References

- Gottesman, S.R., Fenimore, E.E.: New family of binary arrays for coded aperture imaging. *Appl. Opt.* **28**, 4344 (1989)

- Gehm, M.E., McCain, S.T., Pitsianis, N.P., Brady, D.J., Potluri, P., Sullivan, M.E.: Static two-dimensional aperture coding for multimodal, multiplex spectroscopy. *Appl. Opt.* **45**, 2965–2974 (2006)
- Raskar, R., Agrawal, A., Tumblin, J.: Coded exposure photography: Motion deblurring using fluttered shutter. *ACM Trans. Graph.* **25**, 795–804 (2006). <https://doi.org/10.1145/1141911.1141957>
- Chen, E.X., Russell, Z.E., Amsden, J.J., Wolter, S.D., Danell, R.M., Parker, C.B., Stoner, B.R., Gehm, M.E., Glass, J.T., Brady, D.J.: Order of magnitude signal gain in magnetic sector mass spectrometry via aperture coding. *J. Am. Soc. Mass Spectrom.* **26**, 1633–1640 (2015)
- Russell, Z.E., Chen, E.X., Amsden, J.J., Wolter, S.D., Danell, R.M., Parker, C.B., Stoner, B.R., Gehm, M.E., Brady, D.J., Glass, J.T.: Two-dimensional aperture coding for magnetic sector mass spectrometry. *J. Am. Soc. Mass Spectrom.* **26**, 248–256 (2015)
- Russell, Z.E., DiDona, S.T., Amsden, J.J., Parker, C.B., Kibelka, G., Gehm, M.E., Glass, J.T.: Compatibility of spatially coded apertures with a miniature Mattauch-Herzog mass spectrograph. *J. Am. Soc. Mass Spectrom.* **27**, 578–584 (2016)
- Amsden, J.J., Gehm, M.E., Russell, Z.E., Chen, E.X., DiDona, S.T., Wolter, S.D., Danell, R.M., Kibelka, G., Parker, C.B., Stoner, B.R., Brady, D.J., Glass, J.T.: Coded apertures in mass spectrometry. *Annu. Rev. Anal. Chem.* **10**, 141–156 (2017)
- Bleakney, W., Hipple, J.A.: A new mass spectrometer with improved focusing properties. *Phys. Rev.* **53**, 521–529 (1938)
- Robinson, C.F.: Nonuniform fields in cycloidal-focusing mass spectrometers. *Rev. Sci. Instrum.* **27**, 509–512 (1956)
- Amsden, J.J., Herr, P.J., Landry, D.M.W., Kim, W., Vyas, R., Parker, C.B., Kirley, M.P., Keil, A.D., Gilchrist, K.H., Radauscher, E.J., Hall, S.D., Carlson, J.B., Baldasaro, N., Stokes, D., DiDona, S.T., Russell, Z.E., Grego, S., Edwards, S.J., Sperline, R.P., Denton, M.B., Stoner, B.R., Gehm, M.E., Glass, J.T.: Proof of concept coded aperture miniature mass spectrometer using a cycloidal sector mass analyzer, a carbon nanotube (CNT) field emission electron ionization source, and an array detector. *J. Am. Soc. Mass Spectrom.* In preparation (2017)
- Harwit, M., Sloane, N.J.A.: Hadamard transform optics. Academic Press, New York, NY (1979)
- Camilli, R., Hemond, H.F.: NEREUS/Kemonaut, a mobile autonomous underwater mass spectrometer. *TrAC Trends Anal. Chem.* **23**, 307–313 (2004)
- Hemond, H.F.: A backpack-portable mass spectrometer for measurement of volatile compounds in the environment. *Rev. Sci. Instrum.* **62**, 1420–1425 (1991)
- Camilli, R.: Creation and deployment of the NEREUS autonomous underwater chemical analyzer and Kemonaut, an Odyssey class submarine. Thesis, Massachusetts Institute of Technology, Cambridge, MA, USA (2003)
- Adams, N.G., Smith, D.: A multicollector, cycloidal focusing, magnetic mass spectrometer. *J. Phys. E.* **7**, 759 (1974)
- Sahebjavaher, R.S., Walus, K., Stoeber, B.: Permanent magnet desktop magnetic resonance imaging system with microfabricated multitemperature gradient coils for microflow imaging in capillary tubes. *Rev. Sci. Instrum.* **81**, 23706 (2010)
- Halbach, K.: Design of permanent multipole magnets with oriented rare earth cobalt material. *Nucl. Instrum. Methods.* **169**, 1–10 (1980)
- Stelter, R.E.: Dipole permanent magnet structure. US Patent 5635889 (1997)
- Zhang, B., Hatch, G.P.: Field analysis and comparison of several permanent magnet dipole structures. *IEEE Trans. Magn.* **45**, 4395–4398 (2009)
- Voss, G.F., Anthony N. Duryea: Permanent magnet having improved field quality and apparatus employing the same. US Patent 8368496 (2013)
- Blasé, R.C., Miller, G., Westlake, J., Brockwell, T., Ostrom, N., Ostrom, P.H., Waite, J.H.: A compact  $E \times B$  filter: A multi-collector cycloidal focusing mass spectrometer. *Rev. Sci. Instrum.* **86**, 105105 (2015). <https://doi.org/10.1063/1.4932184>
- Radauscher, E.J., Parker, C.B., Gilchrist, K.H., DiDona, S., Russell, Z.E., Hall, S.D., Carlson, J.B., Grego, S., Edwards, S.J., Sperline, R.P., Denton, M.B., Stoner, B.R., Glass, J.T., Amsden, J.J.: A miniature electron ionization source fabricated using microelectromechanical systems (MEMS) with integrated carbon nanotube (CNT) field emission cathodes and low-temperature co-fired ceramics (LTCC). *Int. J. Mass Spectrom.* In Press. (2016). <https://doi.org/10.1016/j.ijms.2016.10.021>